

# Optical Constants of Ices Important to Planetary Science from Laboratory Reflectance Spectroscopy

S. C. Tegler<sup>1,10</sup> , W. M. Grundy<sup>1,2</sup> , M. J. Loeffler<sup>1</sup> , P. D. Tribbitt<sup>1,3</sup> , J. Hanley<sup>1,2</sup> , A. V. Jasko<sup>1,4,5</sup> , H. Dawson<sup>1,6,7</sup> , A. N. Morgan<sup>1</sup> , K. J. Koga<sup>1</sup>, A. O. Madden-Watson<sup>1</sup>, M. D. Gomez<sup>1</sup>, J. K. Steckloff<sup>8</sup> , G. E. Lindberg<sup>9</sup> , S. P. Tan<sup>8</sup> , S. M. Raposa<sup>1</sup>, A. E. Engle<sup>1</sup> , C. L. Thieberger<sup>1</sup> , and D. E. Trilling<sup>1</sup> 

<sup>1</sup> Department of Astronomy and Planetary Science, Northern Arizona University, 527 S. Beaver Street, Flagstaff, AZ 86011, USA; [Stephen.Tegler@nau.edu](mailto:Stephen.Tegler@nau.edu)  
<sup>2</sup> Lowell Observatory, 1400 W. Mars Hill Road, Flagstaff, AZ 86001, USA

<sup>3</sup> Astrochemistry Laboratory, NASA Goddard Space Flight Center, Greenbelt, MD 20771, USA

<sup>4</sup> Department of Astronomy, Case Western Reserve University, 2083 MLK Jr. Drive, Cleveland, OH 44106, USA

<sup>5</sup> Department of Earth and Environmental Sciences, University of Rochester, 227 Hutchinson Hall, Rochester, NY 14627, USA

<sup>6</sup> Department of Earth, Environmental, and Planetary Sciences, Washington University, 1 Brookings Drive, St. Louis, MO 63130, USA

<sup>7</sup> Department of Physics and Astronomy, Purdue University, 525 Northwestern Avenue, W. Lafayette, IN 47907, USA

<sup>8</sup> Planetary Science Institute, 1700 E. Fort Lowell, Suite 106, Tucson, AZ 85719, USA

<sup>9</sup> Department of Chemistry and Biochemistry, Northern Arizona University, 700 S. Osborne Drive, Flagstaff, AZ 86011, USA

Received 2023 August 20; revised 2023 December 14; accepted 2023 December 15; published 2024 February 5

## Abstract

Laboratory-derived optical constants are essential for identifying ices and measuring their relative abundances on solar system objects. Almost all optical constants of ices important to planetary science come from experiments with transmission geometries. Here we describe our new experimental setup and the modification of an iterative algorithm in the literature to measure the optical constants of ices from experiments with reflectance geometries. We apply our techniques to CH<sub>4</sub> ice and H<sub>2</sub>O ice samples and find good agreement between our values and those in the literature, except for one CH<sub>4</sub> band in the literature that likely suffers from saturation. The work we present here demonstrates that labs with reflectance geometries can generate optical constants essential for the proper analysis of near- and mid-infrared spectra of outer solar system objects such as those obtained with the James Webb Space Telescope.

*Unified Astronomy Thesaurus concepts:* [Laboratory astrophysics \(2004\)](#); [Ice spectroscopy \(2250\)](#); [Ice composition \(2272\)](#); [Optical constants \(Ice\) \(2275\)](#); [Physical properties \(Ice\) \(2276\)](#)

## 1. Introduction

Optical constants are essential for identifying and measuring the abundances of molecular ices on the surfaces of solar system objects. Specifically, they are necessary inputs for radiative transfer models that generate synthetic spectra (Hapke 1993; Shkuratov et al. 1999). Comparison of these synthetic spectra to telescope or spacecraft spectra results in the identification and abundance measurements of ices on solar system bodies. For examples, see Cruikshank et al. (1998), Dumas et al. (2007), Merlin et al. (2010), Tegler et al. (2012), and Grundy et al. (2020).

Laboratory techniques to measure the optical constants of molecular ices date back decades. One of the earliest experiments of importance to planetary science was by Bergren et al. (1978), where they established the experimental and iterative computational techniques of extracting optical constants from a single infrared transmission spectrum of a thin-film sample. Subsequent experiments to measure optical constants of importance to planetary science include works by Hagen et al. (1981), Hudgins et al. (1993), Hansen (1997), and Mastrapa et al. (2008, 2009).

Recently, Gerakines & Hudson (2020a) made significant computational improvements to the technique first put forward by Bergren et al. (1978) and Hagen et al. (1981). In addition, they made the point that the literature sometimes exhibits large differences in optical constants for the same material, which may be due to either subtleties in the experimental techniques or differences in the algorithms to extract the optical constants. They further point out that it is impossible to sort out the causes for the differences because few published results provide digital access to the original laboratory data, the algorithm to extract the optical constants from the data, and the resulting optical constants. Gerakines and Hudson made their experimental data, algorithm, and resulting optical constants for dozens of ices available on their website<sup>11</sup> and Zenodo (Gerakines & Hudson 2020b).

It is possible to obtain optical constants of thin films from transmission or reflectance geometries (Tolstoy et al. 2003). In transmission geometry, a vapor deposits as ice onto a cold transparent substrate. The spectrometer beam, nearly normal to the surface of the sample, passes through the ice, then the substrate, and then often through a thinner layer of ice on the back side of the substrate on its way to the detector. In reflectance geometry, a vapor deposits ice onto a highly reflective surface such as gold. The spectrometer beam is likely at an oblique angle to the surface of the ice sample. Part of the beam reflects off the surface of the ice back to the detector. The rest of the beam passes through the sample, reflects off the substrate, passes through the sample again, and finally travels onto the detector. The two parts of the beam

<sup>10</sup> Corresponding author.

 Original content from this work may be used under the terms of the [Creative Commons Attribution 4.0 licence](#). Any further distribution of this work must maintain attribution to the author(s) and the title of the work, journal citation and DOI.

<sup>11</sup> <https://science.gsfc.nasa.gov/691/cosmicice/constants.html>

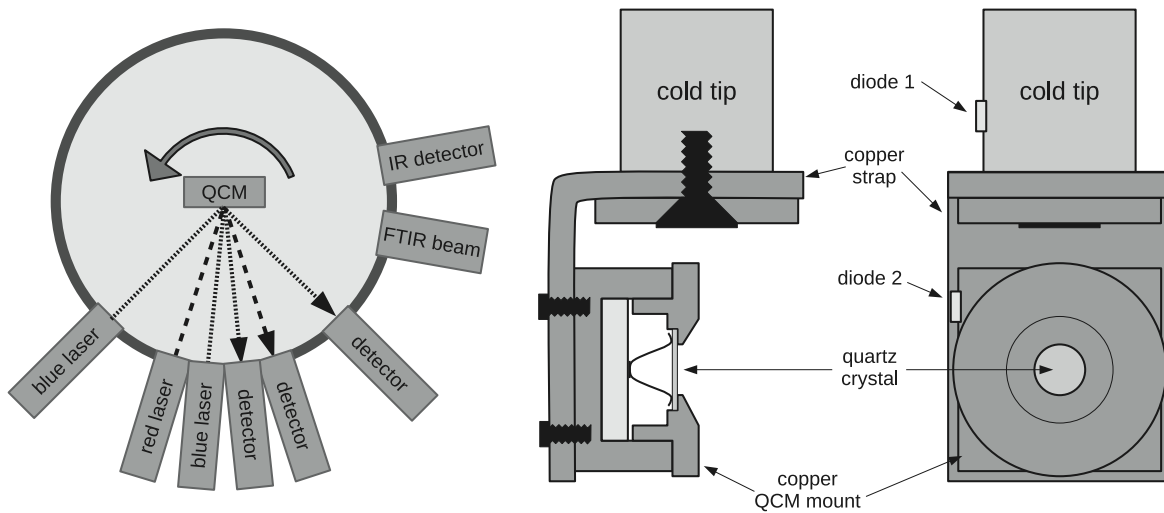


**Figure 1.** The left panel is a view of QCM from above showing its location relative to the lasers, detectors, and FTIR beam in our system. The middle panel is a side view of the QCM. The right panel is a face-on view of the QCM. The middle and right panels show the cold head, two diodes for temperature measurements, copper strap, and QCM mount. Ice is deposited on the gold-plated quartz crystal. For clarity, wiring and indium foil to improve thermal conduction between the copper strap and the copper QCM mount are not shown.

recombine (out of phase) and create channel fringes in the spectrum. Previous optical constant work mostly uses transmission spectroscopy, as the mathematics to extract optical constants from transmission spectra is simpler than the mathematics to extract optical constants from reflectance spectra. For instance, in reflectance geometry the spectrometer beam typically is not perpendicular to the ice surface, making it necessary to account for the *S* and *P* polarization states and work with more intricate Fresnel coefficients.

Although extraction of optical constants is mathematically intricate for reflection spectroscopy, it has advantages. First, we do not have to account for ice on the back side of the substrate as is necessary for transmission geometry. Second, it is possible to irradiate ices with electrons or ions in reflectance geometry and study the resulting solid-state chemistry. Irradiation of transparent substrates may result in electrostatic charging and changes in the substrate properties (Clark & Crawford 1973; Teolis et al. 2007). Third, it is possible to use a quartz crystal microbalance (QCM) as the substrate in reflectance geometry and obtain information about the density of the ice (Westley et al. 1998; Loeffler et al. 2006) and its vapor pressure (Hudson et al. 2022; Grundy et al. 2024). Because of these advantages, we decided to modify the algorithm by Gerakines & Hudson (2020a) for transmission geometry to work in reflection geometry.

Below we describe our experimental setup and algorithm to measure the optical constants of ices in reflectance geometry, applying the algorithm to two ices of importance to planetary science, CH<sub>4</sub> and H<sub>2</sub>O.

## 2. Experimental Setup

We performed experiments in the Astrophysical Materials Laboratory at Northern Arizona University. We pumped on our vacuum chamber with an Agilent TwisTorr 305 FS turbomolecular pump backed up by an Agilent Varian DS302 dual-stage rotary vane roughing pump. The base pressure in the chamber at room temperature was typically  $(1\text{--}2) \times 10^{-8}$  torr. Cryocooling allowed us to reach pressures as low as  $2 \times 10^{-9}$  torr. We used an Agilent variable leak valve (model No. 951-5106) to transfer samples from the reservoir to the vacuum chamber. We background-deposited samples onto the substrate,

while monitoring the pressure ( $\sim 10^{-6}$  torr) with an INFICON Bayard-Alpert Pirani combination gauge sensor (model No. BPG-400).

We deposited our samples onto an INFICON IC6 optically flat, gold-plated QCM attached to an Advanced Research Systems (ARS) DE-204 PB two-stage closed-cycle helium cold head hanging vertically into the vacuum chamber (Figure 1). We measured the temperatures of a sample on the quartz crystal using two temperature-sensitive diodes. The temperature was controlled with a  $50\ \Omega$  heater wrapped around the cold tip and a Lake Shore temperature controller (model 355). We used a copper QCM mount and copper strap to maximize the thermal conductivity between the cold tip and the gold-plated quartz crystal. We were able to cool samples as low as 10 K.

We used a three-laser setup to measure the index of refraction of the sample at the wavelength of the lasers and the thickness of the sample. We placed two blue lasers of wavelengths 0.407 and 0.405  $\mu\text{m}$  at angles  $\theta_1 = 3.7^\circ \pm 1.0^\circ$  and  $\theta_2 = 45.2^\circ \pm 1.0^\circ$  to the normal of the quartz crystal surface while we grew an ice sample. We computed the index of refraction using

$$n_{\text{blue}} = \sqrt{\frac{\sin^2 \theta_2 - \left(\frac{t_1}{t_2}\right)^2 \sin^2 \theta_1}{1 - \left(\frac{t_1}{t_2}\right)^2}}, \quad (1)$$

where  $t_1$  and  $t_2$  were the oscillation periods of the laser signals for the narrow-angle laser and the wide-angle laser, respectively, during deposition of the ice sample (Tempelmeyer & Mills 1968; Satorre et al. 2008; Romanescu et al. 2010; Loeffler et al. 2016).

We calculated the thickness,  $h$ , of the sample in  $\mu\text{m}$  from the number of fringes in the narrow-angle laser signal,  $N_1$ , using

$$h = \frac{N_1 \lambda}{2 \sqrt{n_{\text{blue}}^2 - \sin^2 \theta_1}} \quad (2)$$

(Heavens 1991), where  $\lambda$  is the wavelength of the blue laser (0.407  $\mu\text{m}$ ). For the two CH<sub>4</sub> experiments we report on here, the thicknesses were 0.44 and 1.54  $\mu\text{m}$ . For the H<sub>2</sub>O experiment, the thickness was 0.23  $\mu\text{m}$ .

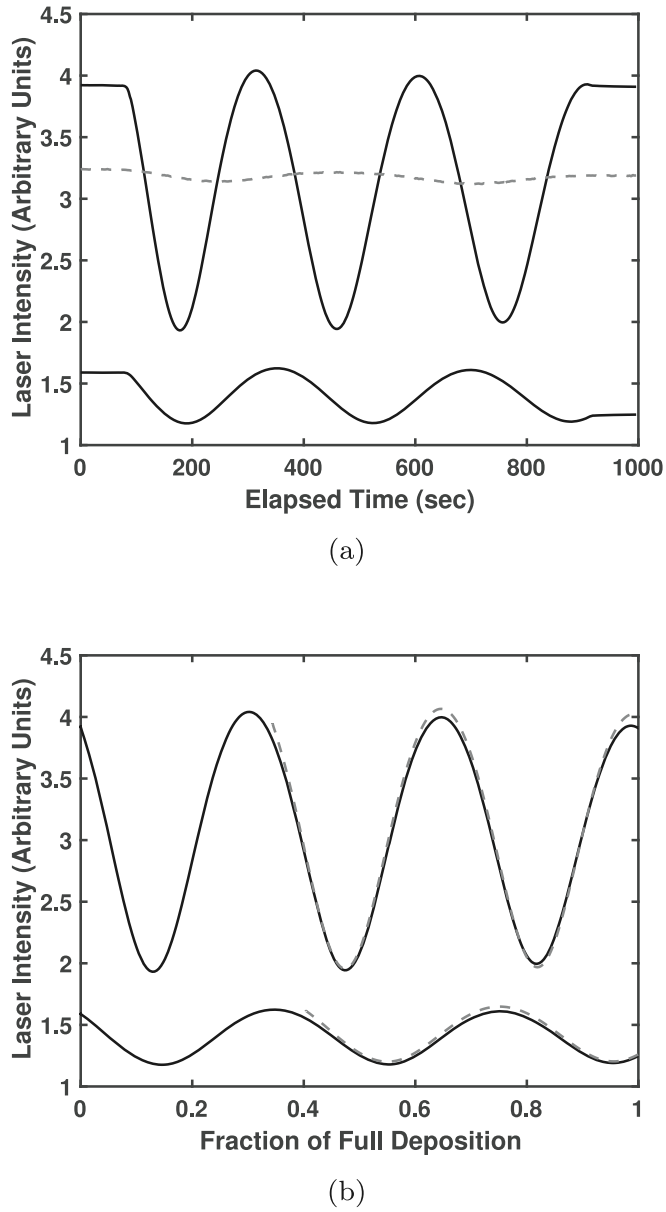


**Figure 2.** Laser interferometry. (a) Intensities of lasers vs. elapsed time of deposition. The two blue lasers at  $\theta_1 = 3.7^\circ$  (top black line) and  $\theta_2 = 45^\circ$  (bottom black line) have more fringes and deeper fringes compared to a red laser at near-normal incidence to the sample surface (dashed black line). (b) Intensities of two blue lasers vs. fraction of full deposition allow us to remove the effects of a variable deposition rate. Original laser signals shifted by one period (dashed black lines) enable us to determine the periods of the laser signals.

Our techniques for measuring  $t_1/t_2$  and  $N_1$  are different from what is published in the literature. First, we used blue lasers rather than red lasers because blue lasers give more fringes and deeper fringes than red lasers. In Figure 2(a), we compare the fringes from the two blue lasers at  $\theta_1 = 3.7^\circ \pm 1.0^\circ$  (top black line) and  $\theta_2 = 45.2^\circ \pm 1.0^\circ$  (bottom black line) to the fringes from a third red laser at near-normal incidence to the sample surface (dashed black line). Second, we used the QCM to change the units on the  $x$ -axis from elapsed time in seconds as seen in Figure 2(a) to the fraction of full deposition,  $x$ , as seen in Figure 2(b). Specifically, the QCM measured a frequency that depended on the deposited mass, where  $f_1$  was the frequency prior to deposition and  $f_2$  was the frequency after

deposition. At each time step,  $i$ , we computed the fraction of full deposition as  $x = (f_1 - f(i))/(f_1 - f_2)$ . The conversion enabled us to remove any effects due to a variable deposition rate. Third, we determined the ratio of laser signal periods,  $t_1/t_2$ , by measuring the number of fringes in each laser signal,  $N_1$  and  $N_2$ . The values  $1/N_1$  and  $1/N_2$  gave the periods of the signals because we plotted each signal against the fraction of full deposition that ranged in value from 0 to 1. To determine the number of fringes for the first laser signal, we repeatedly plotted the original signal ( $x$ , laser-intensity<sub>1</sub>), and the original signal shifted by  $1/N_1 (x + 1/N_1, \text{laser-intensity}_1)$  until we found the value of  $N$  that resulted in the best overplot of the shifted signal on the original signal. We repeated the process for the second laser signal. We show the best-shifted signals in Figure 2(b) as dashed black lines. The ratio of the number of fringes gave us  $t_1/t_2$ ,

$$\frac{t_1}{t_2} = \frac{N_2}{N_1}. \quad (3)$$

We used the QCM to measure the density,  $\rho$ , of our ice sample in  $\text{g cm}^{-3}$ . Specifically, the QCM measured the resonance frequency of the quartz crystal prior to the deposition,  $f_1$ , and at the end of the deposition,  $f_2$ , in Hz. Combining these measured frequencies with our thickness measurement above, we computed the density from

$$\rho = \frac{C}{h} \left( \frac{1}{f_2} - \frac{1}{f_1} \right), \quad (4)$$

where  $C = 4.417 \times 10^5 \text{ Hz g cm}^{-2}$  depends on the density and frequency constant of an AT-cut quartz crystal (Lu & Lewis 1972).

We used a Thermo–Nicolet iS50 Fourier transform infrared (FTIR) spectrometer to generate an external beam. Gold-coated parabolic mirrors focused the beam at an incidence angle of  $8.5^\circ$  to the normal of the sample and upon reflection focused the beam onto a Mercury Cadmium Telluride type A (MCT-A) detector. All experiments covered a wavenumber  $\tilde{\nu}$  (wavelength) range between  $8000 \text{ cm}^{-1}$  ( $1.25 \mu\text{m}$ ) and  $1000 \text{ cm}^{-1}$  ( $10 \mu\text{m}$ ) at a resolution of  $0.5 \text{ cm}^{-1}$ . We averaged 125 scans for each sample and reference (bare substrate) spectrum.

### 3. Reflectance Model

Extraction of optical constants from a reflectance spectrum requires a model that simulates the experimental reflectance data. Teolis et al. (2007) devised such a model; however, they focused on band strengths rather than optical constants and did not publish their code. Here we describe our reflectance model. We assign variables consistent with the Gerakines & Hudson (2020a) transmission model. In particular, we define the optical constants of the thin-film sample as  $m_1(\tilde{\nu}) = n_1(\tilde{\nu}) - ik_1(\tilde{\nu})$ , where  $n_1$  is the real part and  $k_1$  is the imaginary part. In the model, the light at wavenumber  $\tilde{\nu}$  in a vacuum is incident on the surface of the thin film of thickness  $h$  at an angle  $\phi_0$  to the surface normal. Light from the FTIR reflects and refracts at the interfaces on its way to the detector as shown in Figure 3. We denote quantities associated with the vacuum, film, and substrate with the subscripts 0, 1, and 2, respectively. Because the incident light is not normal to the surface, we must account for the  $S$  and  $P$  polarization states. We assume unpolarized light, and so we assign equal weights to the  $P$ - and  $S$ -states, where the  $P$ -state is the component of light that has its electric

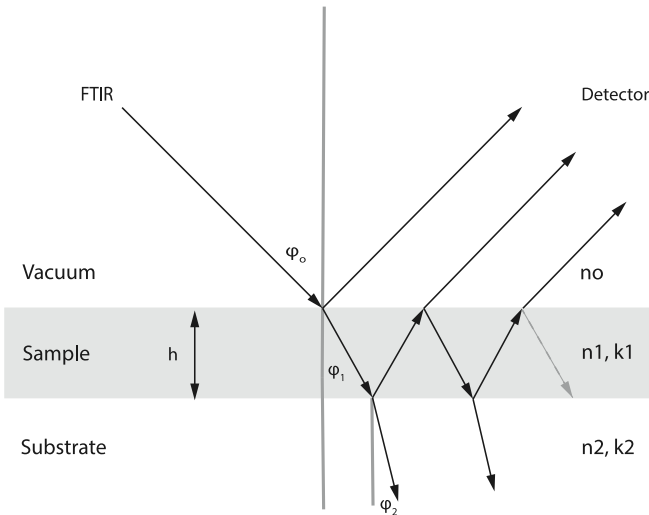


**Figure 3.** Quantities in the reflection model and the path of light from the FTIR, through the sample, and onto the detector.

field parallel to the ice surface and the *S*-state is the component that has its electric field perpendicular to the surface.

Because we need to divide the experimental sample spectrum by the reference spectrum to remove instrumental effects, our model computes the reflectance spectrum from the ice-covered substrate divided by the reflectance spectrum from the bare substrate, i.e., the reflectance ratio,  $R$ , given by

$$R = \frac{R^P + R^S}{|r_{20}^P|^2 + |r_{20}^S|^2}, \quad (5)$$

where

$$R^P = \left| \frac{r_1^P + r_2^P e^{-2i\delta_1}}{1 + r_1^P r_2^P e^{-2i\delta_1}} \right|^2 \quad (6)$$

and

$$R^S = \left| \frac{r_1^S + r_2^S e^{-2i\delta_1}}{1 + r_1^S r_2^S e^{-2i\delta_1}} \right|^2. \quad (7)$$

The lowercase  $r$  symbols represent the Fresnel coefficients. The coefficients  $r_1^P$  and  $r_1^S$  represent the amplitude of *P*-state light and *S*-state light reflected at the vacuum–ice interface and are given by

$$r_1^P = \frac{m_0 \cos \phi_1 - m_1 \cos \phi_0}{m_0 \cos \phi_1 + m_1 \cos \phi_0}, \quad (8)$$

$$r_1^S = \frac{m_0 \cos \phi_0 - m_1 \cos \phi_1}{m_0 \cos \phi_0 + m_1 \cos \phi_1}. \quad (9)$$

The coefficients  $r_2^P$  and  $r_2^S$  represent the amplitude of *P*-state light and *S*-state light reflected at the ice–substrate interface and are given by

$$r_2^P = \frac{m_1 \cos \phi_2 - m_2 \cos \phi_1}{m_1 \cos \phi_2 + m_2 \cos \phi_1}, \quad (10)$$

$$r_2^S = \frac{m_1 \cos \phi_1 - m_2 \cos \phi_2}{m_1 \cos \phi_1 + m_2 \cos \phi_2}. \quad (11)$$

The coefficients  $r_{20}^P$  and  $r_{20}^S$  represent the amplitude of *P*-state light and *S*-state light reflected at the vacuum–substrate

interface and are given by

$$r_{20}^P = \frac{m_0 \cos \phi_{20} - m_2 \cos \phi_0}{m_0 \cos \phi_{20} + m_2 \cos \phi_0}, \quad (12)$$

$$r_{20}^S = \frac{m_0 \cos \phi_0 - m_2 \cos \phi_{20}}{m_0 \cos \phi_0 + m_2 \cos \phi_{20}}. \quad (13)$$

It is important to recognize that  $m_0$ ,  $m_1$ , and  $m_2$  are the optical constants for vacuum, the ice film, and substrate, respectively, and are complex functions given by

$$m_0 = n_0 - ik_0, \quad (14)$$

$$m_1 = n_1(\tilde{\nu}) - ik_1(\tilde{\nu}), \quad (15)$$

$$m_2 = n_2(\tilde{\nu}) - ik_2(\tilde{\nu}). \quad (16)$$

The optical constants  $n_0 = 1$  and  $k_0 = 0$  are for vacuum. The optical constants  $n_2$  and  $k_2$  are for the gold substrate (Babar & Weaver 2015).

The trigonometric values  $\cos \phi_1$ ,  $\cos \phi_2$ , and  $\cos \phi_{20}$  come from the complex version of Snell’s law and are given by

$$\cos \phi_1 = \left( 1 - \frac{\sin^2 \phi_0}{n_1^2 - k_1^2 - 2in_1k_1} \right)^{1/2}, \quad (17)$$

$$\cos \phi_2 = \left( 1 - \frac{n_1^2 - k_1^2 - 2in_1k_1}{n_2^2 - k_2^2 - 2in_2k_2} \sin^2 \phi_1 \right)^{1/2}, \quad (18)$$

$$\cos \phi_{20} = \left( 1 - \frac{\sin^2 \phi_0}{n_2^2 - k_2^2 - 2in_2k_2} \right)^{1/2}. \quad (19)$$

Finally,  $\delta_1$  is the change in phase of the beam on traversing the film and is given by

$$\delta_1 = 2\pi\tilde{\nu}m_1h \cos \phi_1. \quad (20)$$

See Heavens (1991) for derivations of Equations (6)–(13) and (20).

#### 4. Iterative Algorithm

It is not possible to invert Equation (5) and analytically solve for  $n_1(\tilde{\nu})$  and  $k_1(\tilde{\nu})$ . Rather, the canonical approach, most recently described and modified by Gerakines & Hudson (2020a), is to compare the model spectrum to the experimental spectrum and make iterative changes to the values of  $n_1(\tilde{\nu})$  and  $k_1(\tilde{\nu})$  in the model until the model spectrum closely approximates the experimental spectrum. We briefly outline the canonical method, while focusing on modifications we made to the Gerakines and Hudson Python code that is available on their website.

First, we collected the necessary inputs for the algorithm, i.e., our measurements of  $h$ ,  $n_{\text{blue}}$ , and the experimental reflectance ratio,  $R_{\text{lab}}$ , as well as the published optical constants for gold,  $n_2(\tilde{\nu})$  and  $k_2(\tilde{\nu})$ , from Babar & Weaver (2015). Next, we set  $n_1(\tilde{\nu}) = n_{\text{blue}}$  and  $k_1(\tilde{\nu}) = 0$ . Then, we used the reflectance model described in Section 3 to compute the first model spectrum,  $R$ . Just like Gerakines & Hudson (2020a), we next computed a first improvement to  $k_1$  using the Newton–Raphson root-finding method, i.e.,  $\Delta k_1$ , given by

$$\Delta k_1 = \frac{\ln R_{\text{lab}} - \ln R(n_1, k_1)}{(\partial \ln R / \partial k_1)|_{n_1, k_1}}. \quad (21)$$

Because of the complexity of  $R$  for reflectance at oblique incidence, we used a numerical approximation to the partial

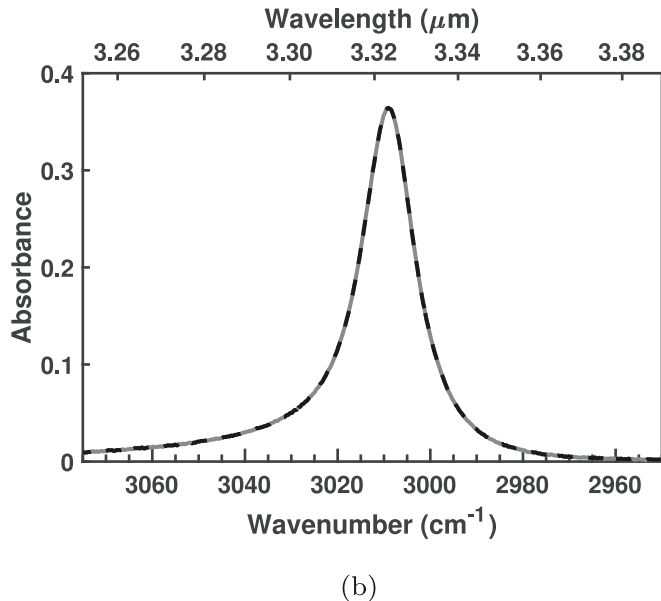


**Figure 4.** Comparison between experimental absorbance (dashed black line) and model (gray line) for the  $\text{CH}_4 \nu_3$  band at  $3011 \text{ cm}^{-1}$ .

derivative in the denominator of Equation (21). We note that the analytical expression used by Gerakines and Hudson for this partial derivative only applies to a transmission experiment at normal incidence. After replacing  $k_1$  with  $k_1 + \Delta k_1$ , we used an approximation to a Kramers–Kronig relation to compute a new  $n_1$  at each wavenumber  $\tilde{\nu}_i$  of the spectrum,

$$n_1(\tilde{\nu}_i) \approx n_{\text{blue}} + \frac{2}{\pi} \int_{\text{ir}} \frac{\tilde{\nu} k_1(\tilde{\nu})}{\tilde{\nu}^2 - \tilde{\nu}_i^2} d\tilde{\nu}. \quad (22)$$

We note that if the ice has a strong absorption band between the wavelength of the blue laser and where the integration begins in Equation (22), the approximation could break down. However, in our case, neither  $\text{CH}_4$  nor  $\text{H}_2\text{O}$  discussed below has strong absorption bands in this region.

Next, we computed a second model  $R$  and compared it to  $R_{\text{lab}}$ . Then, we computed the fractional deviation between the model and experimental spectrum at each  $\tilde{\nu}$ ,

$$\frac{|R_{\text{lab}} - R(n_1, k_1)|}{R_{\text{lab}}}. \quad (23)$$

We then recalculated new values of  $n_1$  and  $k_1$  using Equations (21) and (22) and subsequent values of  $R$  and the fractional deviation. We repeated the process until the fractional deviation was  $< 1.0 \times 10^{-5}$  at every  $\tilde{\nu}$ .

In short, we modified the Python code of Gerakines & Hudson (2020a) to include the reflection physics in Section 3, gold optical constants for the substrate, and a numerical approximation to the denominator in Equation (21). The rest of the code is the same as the Gerakines and Hudson code, and their Figure 2 provides a flow chart of the overall algorithm.

## 5. Results

### 5.1. $\text{CH}_4$

In this section, we describe our measurements of  $n_{\text{blue}}$ ,  $\rho$ ,  $n_1(\tilde{\nu})$ , and  $k_1(\tilde{\nu})$  for  $\text{CH}_4$ . In each experiment, we obtained a

**Table 1**  
Index of Refraction and Density of Crystalline  $\text{CH}_4$

Phase	$T$ (K)	$\lambda$ (nm)	$n_{\text{vis}}$	$\rho$ ( $\text{g cm}^{-3}$ )	References
Crystal II	10	0.407	$1.34 \pm 0.02$	$0.49 \pm 0.01$	1
Crystal II	10	0.633	1.30	0.47	2
Crystal I	30	0.633	1.30	0.47	2
Crystal I	30	0.628	1.36	0.45	3

**References.** (1) This work; (2) Satorre et al. (2008); (3) Molpeceres et al. (2017).

spectrum of the bare substrate and recorded the laser and QCM signals while we background-deposited the  $\text{CH}_4$  ice at 10 K.

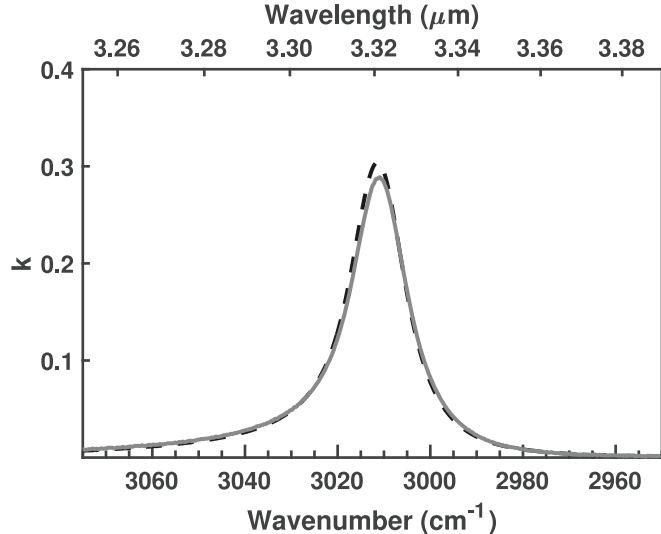
$\text{CH}_4$  ice has three different phases between 10 and 30 K: amorphous, crystalline II, and crystalline I. Using profiles of the  $\nu_4$  band near  $1300 \text{ cm}^{-1}$ , Gerakines & Hudson (2015) showed that the formation of amorphous  $\text{CH}_4$  required a slow deposition rate at temperatures below 20 K, and crystalline II resulted from a fast deposition rate below 20 K. Warming crystalline II ice from 10 to 30 K formed crystalline I ice.

In our experiments, we wanted to measure optical constants for crystalline I  $\text{CH}_4$  and compare them to values reported by Gerakines & Hudson (2020a). We quickly deposited at 10 K, obtaining  $n_{\text{blue}}$  and  $\rho$ . A spectrum of each sample at 10 K showed a  $\nu_4$  band with a double peak, confirming crystalline II ice. Next, we warmed the sample  $4 \text{ K minute}^{-1}$  to 30 K. The spectra showed a symmetric  $\nu_4$  band, confirming that we had crystalline I ice.

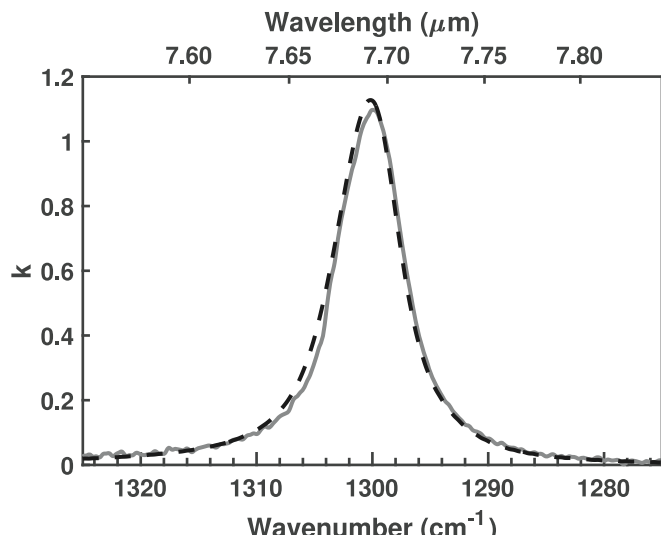
In Table 1, we present our measurements for the index of refraction and density of  $\text{CH}_4$  compared to previous work. We measure  $n_{\text{blue}} = 1.34 \pm 0.02$  for  $\text{CH}_4$  deposited at 10 K. The uncertainty in  $n_{\text{blue}}$  is dominated by the uncertainty in our measurement of  $\theta_2$ . Given the scatter of the index of refraction values in the work of Satorre et al. (2008, their Figure 3), we conclude that our measurement for the index of refraction is consistent with their measurement. Our density measurement is  $\rho = 0.49 \pm 0.01 \text{ g cm}^{-3}$  at 10 K. The uncertainty is the standard deviation of values from five experiments. From Table 1, we see that our density measurement is in good agreement with Satorre et al.

In Figure 4, we compare our measured spectrum to our best-fit model for the  $\text{CH}_4 \nu_3$  band at  $3011 \text{ cm}^{-1}$ . We make the comparison in absorbance, i.e.,  $-\log_{10}(R_{\text{sam}}/R_{\text{ref}})$  to  $-\log_{10} R$ , where  $(R_{\text{sam}}/R_{\text{ref}})$  is the sample spectrum divided by the reference spectrum (dashed black line) and  $R$  is the model spectrum from Equation (5) (gray line). There is excellent agreement between the experimental and model spectra.

In Figures 5(a) and (b), we plot the imaginary part of the optical constants,  $k_1(\tilde{\nu})$ , for the  $\nu_3$  ( $3011 \text{ cm}^{-1}$ ) and  $\nu_4$  ( $1300 \text{ cm}^{-1}$ ) vibrational modes (gray line). These  $k$ -values come from our reflection spectrum of a  $0.44 \mu\text{m}$  thick sample and the reflectance model described above. In addition, we overplot  $k$ -values from Gerakines & Hudson (2020a; dashed black line) for a sample deposited at 10 K and warmed to 30 K. Despite the difference in reflection and transmission geometries, there is excellent agreement between the  $k$ -spectra. The agreement confirms consistent experimental and modeling procedures for both groups, as well as providing confidence in these  $k$ -values for radiation transfer modeling of outer solar system objects.



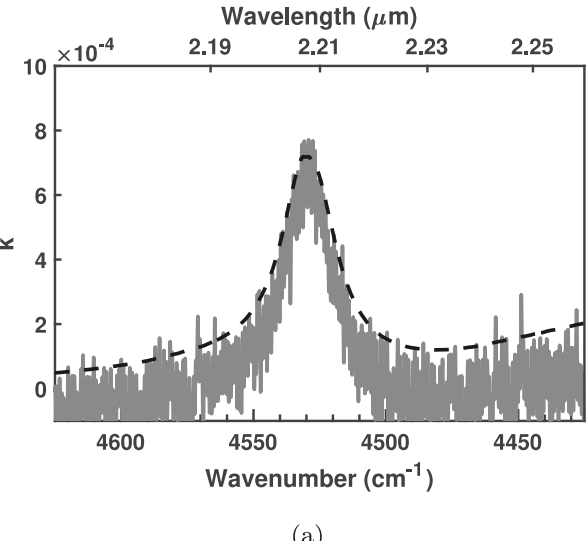
(a)



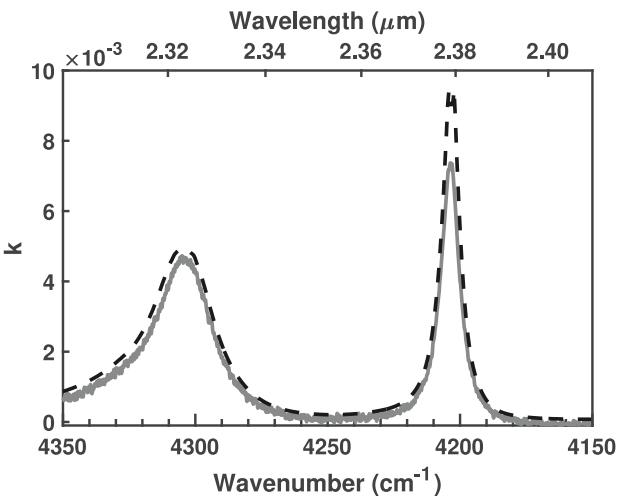
(b)

**Figure 5.** Comparison between our  $k$ -values (gray lines) and Gerakines & Hudson (2020a)  $k$ -values (dashed black lines) for  $\text{CH}_4$  at 30 K. (a) The  $\nu_3$  band at  $3011 \text{ cm}^{-1}$ . (b) The  $\nu_4$  band at  $1300 \text{ cm}^{-1}$ .

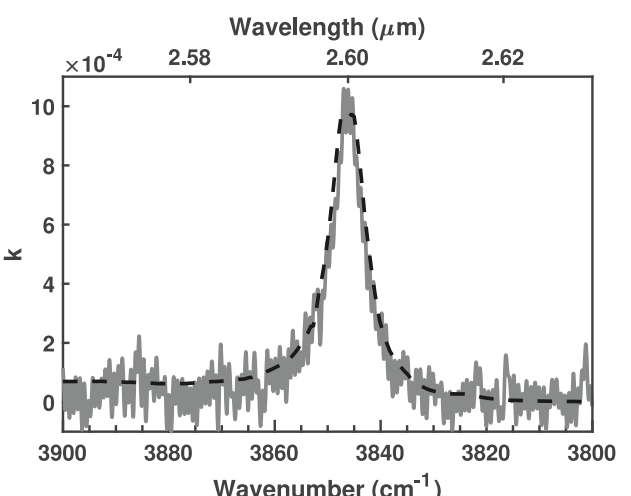
In Figures 6(a)–(c), we plot our  $k$ -values for a thicker  $1.54 \mu\text{m}$   $\text{CH}_4$  sample so as to study the intrinsically weaker overtones and combination bands of  $\text{CH}_4$ . We compare our  $k$ -values (gray lines) to the  $k$ -values of Grundy et al. (2002) (dashed black lines). Unsurprisingly, the Grundy values exhibit a much higher signal-to-noise ratio than our values owing to the much larger thicknesses of their samples. However, there is good agreement between the two sets of  $k$ -values. We note that the  $\nu_2 + \nu_3$  band in Figure 6(a) is more than 1000 times weaker than the  $\nu_4$  band plotted in Figure 5(b). In Figure 6(b), we plot the  $k$ -values for the  $\nu_3 + \nu_4$  band at  $4303 \text{ cm}^{-1}$  and the  $\nu_1 + \nu_4$  band at  $4203 \text{ cm}^{-1}$ . We find good agreement between our values and the Grundy values for the  $\nu_3 + \nu_4$  band; however, we find a significant disagreement in the  $\nu_1 + \nu_4$  band. The double peak at the top of the  $\nu_1 + \nu_4$  band in the Grundy spectrum suggests saturation of the band. In Figure 6(c), we



(a)



(b)



(c)

**Figure 6.** Comparison between our  $k$ -values (gray lines) and Grundy et al. (2002)  $k$ -values (dashed black lines) for  $\text{CH}_4$  at 30 K. (a) The  $\nu_2 + \nu_3$  band at  $4530 \text{ cm}^{-1}$ . (b) The  $\nu_3 + \nu_4$  band at  $4303 \text{ cm}^{-1}$  and the  $\nu_1 + \nu_4$  band at  $4203 \text{ cm}^{-1}$ . (c) The  $3\nu_4$  band at  $3846 \text{ cm}^{-1}$ .

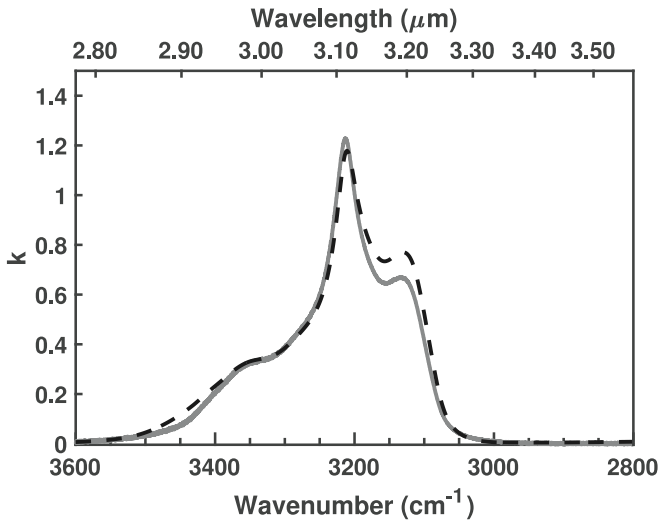


**Figure 7.** Imaginary part of the optical constants,  $k$ , as a function of wavenumber and wavelength for crystalline H<sub>2</sub>O at 50 K from this work (gray line) and Mastrapa et al. (2008; dashed black line). Shown are the 3350 cm<sup>-1</sup> (2.99  $\mu\text{m}$ )  $\nu_3$  LO mode, the 3200 cm<sup>-1</sup> (3.1  $\mu\text{m}$ )  $\nu_3$  TO mode, and the 3100 cm<sup>-1</sup> (3.2  $\mu\text{m}$ )  $\nu_1$  mode.

plot the  $k$ -values for the  $3\nu_4$  band at 3846 cm<sup>-1</sup>. Again, we find good agreement between our values and the Grundy values, despite the much lower signal-to-noise ratio of our much thinner sample. In summary, we find good agreement with the Grundy  $k$ -values, except for the  $\nu_1 + \nu_4$  band at 4203 cm<sup>-1</sup>, where our thinner sample assures no saturation.

## 5.2. H<sub>2</sub>O

Our experimental setup is capable of studying materials that are liquids at room temperature. Here we describe our measurements of  $n_{\text{blue}}$ ,  $\rho$ ,  $n_1(\tilde{\nu})$ , and  $k_1(\tilde{\nu})$  for crystalline H<sub>2</sub>O.

Our sample preparation was as follows. We removed dissolved air in our purified liquid H<sub>2</sub>O with a freeze-pump-thaw process. Because an initially cold amorphous H<sub>2</sub>O sample heated past the amorphous–crystalline phase change at  $\sim$ 135 K can retain significant amounts of amorphous ice (Jenniskens et al. 1998), we deposited our samples at 150 K to ensure a crystalline sample.

For the index of refraction, we measured  $n_{\text{blue}} = 1.36 \pm 0.02$ . The uncertainty in  $n_{\text{blue}}$  is dominated by the uncertainty in  $\theta_2$ . Hudgins et al. (1993) cited values of 1.26–1.35 in the literature for amorphous and crystalline H<sub>2</sub>O and used a value of 1.32. Westley et al. (1998) measured  $1.29 \pm 0.01$  that was independent of deposition temperature between 30 and 140 K. Mastrapa et al. (2008, 2009) cited  $n = 1.32$  at the wavelength of their laser from Hale & Querry (1973) for crystalline H<sub>2</sub>O; however, the reference is for liquid H<sub>2</sub>O at 298 K.

For density, we measured  $\rho = 0.95 \pm 0.01 \text{ g cm}^{-3}$ . Narten et al. (1976) used X-ray diffraction data to measure  $\rho = 0.94 \text{ g cm}^{-3}$  for amorphous ice at 77 K. Westley et al. (1998) measured  $\rho = 0.82 \pm 0.01 \text{ g cm}^{-3}$  for thin films vapor-deposited between 30 and 140 K. Hobbs (1974) reported  $\rho = 0.92 \text{ g cm}^{-3}$  for hexagonal ice.

H<sub>2</sub>O bands span orders of magnitude in their absorption efficiency and so require a range of thicknesses to avoid saturation of the bands. We chose to study the feature near 3200 cm<sup>-1</sup> (3.1  $\mu\text{m}$ ) because of its large absorption efficiency and importance to planetary science. The feature is such a

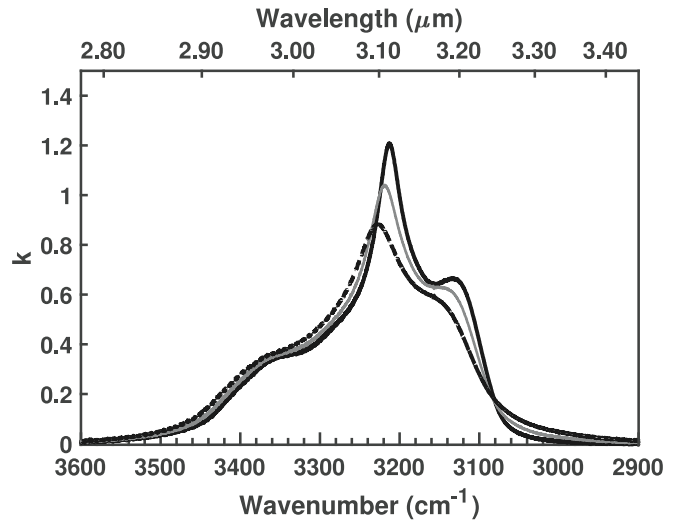


**Figure 8.** Imaginary part of the optical constants,  $k$ , as a function of wavenumber and wavelength for the 3350 cm<sup>-1</sup> (2.99  $\mu\text{m}$ )  $\nu_3$  LO mode, the 3200 cm<sup>-1</sup> (3.1  $\mu\text{m}$ )  $\nu_3$  TO mode, and the 3100 cm<sup>-1</sup> (3.2  $\mu\text{m}$ )  $\nu_1$  mode of crystalline H<sub>2</sub>O at 150 K (dashed black line), 100 K (gray line), and 50 K (black line).

strong absorber that it required a very thin sample corresponding to about one interference fringe, thereby preventing us from using the method described above for measuring the thickness of the sample. Hence, we used our average density and the initial and final QCM frequencies for depositing the thin sample, and we rearranged Equation (4) to solve for thickness. We measured a sample thickness of 0.23  $\mu\text{m}$ . This technique was used by Loeffler et al. (2020) to measure the thicknesses of very thin H<sub>2</sub>O samples. We cooled the sample from 150 to 10 K and collected spectra at intervals of 10 K.

In Figure 7, we plot our  $k$ -values for the 3350 cm<sup>-1</sup> (2.99  $\mu\text{m}$ )  $\nu_3$  LO mode, the 3200 cm<sup>-1</sup> (3.1  $\mu\text{m}$ )  $\nu_3$  TO mode, and the 3100 cm<sup>-1</sup> (3.2  $\mu\text{m}$ )  $\nu_1$  mode (gray line) and compare them to those of Mastrapa et al. (2009; dashed black line). We found good agreement between the two sets of  $k$ -values for the 3350 cm<sup>-1</sup> (2.99  $\mu\text{m}$ ) and 3200 cm<sup>-1</sup> (3.1  $\mu\text{m}$ ), bands; however, there was a small difference between the  $k$ -values for the 3100 cm<sup>-1</sup> (3.2  $\mu\text{m}$ ) band. Perhaps the small differences are due to Mastrapa computing  $k$ -values from their transmission spectrum and then using the Kramers–Kroning relation to compute  $n$  rather than the iterative approach described here.

In Figure 8, we plot  $k$ -values for the 3350 cm<sup>-1</sup> (2.99  $\mu\text{m}$ ), 3200 cm<sup>-1</sup> (3.1  $\mu\text{m}$ ), and 3100 cm<sup>-1</sup> (3.2  $\mu\text{m}$ ) bands of crystalline H<sub>2</sub>O at temperatures of 150 K (dashed black line), 100 K (gray line), and 50 K (black line). As the temperature cools, the 3200 cm<sup>-1</sup> (3.1  $\mu\text{m}$ ) band becomes stronger and shifts to smaller wavenumbers (larger wavelengths) and the 3100 cm<sup>-1</sup> (3.2  $\mu\text{m}$ ) band becomes more pronounced in the spectrum. Similar behavior was seen for these bands in Figure 5 of Mastrapa et al. (2009).

## 6. Conclusions

We described our experimental setup and a modification of the algorithm by Gerakines & Hudson (2020a) to compute optical constants from reflectance spectroscopy. We applied our experimental techniques and algorithm to CH<sub>4</sub> ice at 30 K. We found good agreement with optical constants by Gerakines & Hudson (2020a) and Grundy et al. (2002), except for the  $\nu_1 + \nu_4$  band at 4203 cm<sup>-1</sup>, where their band profile suggests

saturation. The overall good agreement with the literature gives us confidence in our experimental techniques and our modification of the Gerakines and Hudson algorithm. We applied the modified algorithm to our experiments on crystalline H<sub>2</sub>O ice at 50 K. The resulting *k*-values for the 3200 cm<sup>-1</sup> (3.1  $\mu$ m) feature compared well with Mastrapa et al. (2008).

We demonstrated that our experimental setup and modifications to the Gerakines & Hudson (2020a) algorithm are capable of computing optical constants consistent with what is published in the literature. Our laboratory data, modified Python algorithm, and optical constants discussed in this paper are available at the OpenKnowledge@NAU archive.<sup>12</sup> These tools will be of use in computing optical constants essential for modeling the near- and mid-infrared spectra of outer solar system objects obtained with the James Webb Space Telescope.

### Acknowledgments

NASA SSW grant 80NSSC19K0556 provided support for this work. The Arizona Board of Regents Technology Research Initiative Fund (TRIF) provided funds for the purchase of equipment. The National Science Foundation Research Experience for Undergraduates Program at Northern Arizona University (NSF award No. 1950901) and the Northern Arizona University Division of the Arizona Space Grant Consortium (NASA award No. 80NSSC20M0041) provided financial support for the undergraduate researchers. We thank Dr. Perry Gerakines for helpful discussions about his algorithm.

### ORCID iDs

S. C. Tegler  <https://orcid.org/0000-0002-6794-495X>  
 W. M. Grundy  <https://orcid.org/0000-0002-8296-6540>  
 M. J. Loeffler  <https://orcid.org/0000-0002-1551-3197>  
 P. D. Tribbett  <https://orcid.org/0000-0001-9529-8353>  
 J. Hanley  <https://orcid.org/0000-0002-0801-7654>  
 A. V. Jasko  <https://orcid.org/0000-0002-6244-9669>  
 H. Dawson  <https://orcid.org/0000-0002-2047-564X>  
 A. N. Morgan  <https://orcid.org/0000-0001-5932-9570>  
 J. K. Steckloff  <https://orcid.org/0000-0002-1717-2226>  
 G. E. Lindberg  <https://orcid.org/0000-0002-5292-4200>  
 S. P. Tan  <https://orcid.org/0000-0003-2049-3706>  
 A. E. Engle  <https://orcid.org/0000-0002-7894-7056>  
 C. L. Thieberger  <https://orcid.org/0000-0001-7399-434X>  
 D. E. Trilling  <https://orcid.org/0000-0003-4580-3790>

### References

Babar, S., & Weaver, J. H. 2015, *ApOpt*, **54**, 477  
 Bergren, M. S., Schuh, D., Sceats, M. G., & Rice, S. A. 1978, *JChPh*, **69**, 3477  
 Clark, C. D., & Crawford, J. H. 1973, *AdPhy*, **22**, 117  
 Cruikshank, D. P., Roush, T. L., Bartholomew, M. J., et al. 1998, *Icar*, **135**, 389  
 Dumas, C., Merlin, F., Barucci, M. A., et al. 2007, *A&A*, **471**, 331  
 Gerakines, P. A., & Hudson, R. L. 2015, *ApJL*, **805**, L20  
 Gerakines, P. A., & Hudson, R. L. 2020a, *ApJ*, **901**, 52  
 Gerakines, P. A., & Hudson, R. L. 2020b, A Computational Package for the Determination of Infrared Optical Constants Relevant to Astrophysics, Zenodo, doi:10.5281/ZENODO.4429276  
 Grundy, W., Tegler, S., Steckloff, J., et al. 2024, *Icaurs*, **410**, 115767  
 Grundy, W. M., Bird, M. K., Britt, D. T., et al. 2020, *Sci*, **367**, aay3705  
 Grundy, W. M., Schmitt, B., & Quirico, E. 2002, *Icar*, **155**, 486  
 Hagen, W., Tielens, A. G. G. M., & Greenberg, J. M. 1981, *CP*, **56**, 367  
 Hale, G. M., & Querry, M. R. 1973, *ApOpt*, **12**, 555  
 Hansen, G. B. 1997, *JGR*, **102**, 21569  
 Hapke, B. 1993, Theory of Reflectance and Emittance Spectroscopy (Cambridge: Cambridge Univ. Press)  
 Heavens, O. 1991, Optical Properties of Thin Solid Films (2nd ed.; New York: Dover)  
 Hobbs, P. V. 1974, Ice Physics (Oxford: Oxford Univ. Press)  
 Hudgins, D. M., Sandford, S. A., Allamandola, L. J., & Tielens, A. G. G. M. 1993, *ApJS*, **86**, 713  
 Hudson, R. L., Yarnall, Y. Y., & Gerakines, P. A. 2022, *PSJ*, **3**, 120  
 Jenniskens, P., Blake, D. F., & Kouchi, A. 1998, in Solar System Ices, Astrophysics and Space Science Library, Vol. 227, ed. B. Schmitt, C. de Bergh, & M. Festou (Dordrecht: Kluwer), 139  
 Loeffler, M. J., Moore, M. H., & Gerakines, P. A. 2016, *ApJ*, **827**, 98  
 Loeffler, M. J., Teolis, B. D., & Baragiola, R. A. 2006, *ApJL*, **639**, L103  
 Loeffler, M. J., Tribbett, P. D., Cooper, J. F., & Sturmer, S. J. 2020, *Icar*, **351**, 113943  
 Lu, C.-S., & Lewis, O. 1972, *JAP*, **43**, 4385  
 Mastrapa, R. M., Bernstein, M. P., Sandford, S. A., et al. 2008, *Icar*, **197**, 307  
 Mastrapa, R. M., Sandford, S. A., Roush, T. L., Cruikshank, D. P., & Dalle Ore, C. M. 2009, *ApJ*, **701**, 1347  
 Merlin, F., Barucci, M. A., de Bergh, C., et al. 2010, *Icar*, **208**, 945  
 Molpeceres, G., Satorre, M. A., Ortigoso, J., et al. 2017, *MNRAS*, **466**, 1894  
 Narten, A. H., Venkatesh, C. G., & Rice, S. A. 1976, *JChPh*, **64**, 1106  
 Romanescu, C., Marschall, J., Kim, D., Khatiwada, A., & Kalogerakis, K. S. 2010, *Icar*, **205**, 695  
 Satorre, M. A., Domingo, M., Millán, C., et al. 2008, *P&SS*, **56**, 1748  
 Shkuratov, Y. G., Kreslavsky, M. A., Ovcharenko, A. A., et al. 1999, *Icar*, **141**, 132  
 Tegler, S. C., Grundy, W. M., Olkin, C. B., et al. 2012, *ApJ*, **751**, 76  
 Tempelmeyer, K. E., & Mills, D. W. J. 1968, *JAP*, **39**, 2968  
 Teolis, B. D., Loeffler, M. J., Raut, U., Famá, M., & Baragiola, R. A. 2007, *Icar*, **190**, 274  
 Tolstoy, V. P., Chernyshova, I., & Skryshevsky, V. A. 2003, Handbook of Infrared Spectroscopy of Ultrathin Films (Hoboken, NJ: Wiley)  
 Westley, M. S., Baratta, G. A., & Baragiola, R. A. 1998, *JChPh*, **108**, 3321

<sup>12</sup> <https://openknowledge.nau.edu/id/eprint/6249>